Thermal performance of a flat polymer heat pipe heat spreader under high acceleration

2012 J. Micromech. Microeng. 22 045018

(http://iopscience.iop.org/0960-1317/22/4/045018)

J. Micromech. Microeng. **22** (2012) 045018 (12pp) doi:10.1088/0960-1317/22/4/045018

Thermal performance of a flat polymer heat pipe heat spreader under high acceleration

Christopher Oshman[1], Qian Li[1], Li-Anne Liew[1], Ronggui Yang[1], Y C Lee[1], Victor M Bright[1], Darin J Sharar[2], Nicholas R Jankowski[3] and Brian C Morgan[3]

[1] Department of Mechanical Engineering, University of Colorado, Boulder, CO, USA
[2] General Technical Services, LLC, Wall, NJ, USA
[3] U.S. Army Research Laboratory, Adelphi, MD, USA

E-mail: victor.bright@colorado.edu

Received 8 November 2011, in final form 31 January 2012
Published 19 March 2012
Online at stacks.iop.org/JMM/22/045018

Abstract

This paper presents the fabrication and application of a micro-scale hybrid wicking structure in a flat polymer-based heat pipe heat spreader, which improves the heat transfer performance under high adverse acceleration. The hybrid wicking structure which enhances evaporation and condensation heat transfer under adverse acceleration consists of 100 μm high, 200 μm wide square electroplated copper micro-pillars with 31 μm wide grooves for liquid flow and a woven copper mesh with 51 μm diameter wires and 76 μm spacing. The interior vapor chamber of the heat pipe heat spreader was $30 \times 30 \times 1.0$ mm^3. The casing of the heat spreader is a 100 μm thick liquid crystal polymer which contains a two-dimensional array of copper-filled vias to reduce the overall thermal resistance. The device performance was assessed under 0–10 g acceleration with 20, 30 and 40 W power input on an evaporator area of 8×8 mm^2. The effective thermal conductivity of the device was determined to range from 1653 W (m K)$^{-1}$ at 0 g to 541 W (m K)$^{-1}$ at 10 g using finite element analysis in conjunction with a copper reference sample. In all cases, the effective thermal conductivity remained higher than that of the copper reference sample. This work illustrates the possibility of fabricating flexible, polymer-based heat pipe heat spreaders compatible with standardized printed circuit board technologies that are capable of efficiently extracting heat at relatively high dynamic acceleration levels.

(Some figures may appear in colour only in the online journal)

Nomenclature

A_{Al}	condenser bar cross-sectional area (m^2)
A_w	wick cross-sectional area (m^2)
D_h	hydraulic diameter (m)
δ	groove height (m)
ε	porosity
$\mathrm{fRe}_{L,h}$	friction Reynolds number
g	gravitational acceleration (m s^{-2})
k	thermal conductivity (W (m K)$^{-1}$)
K	permeability (m^2)
L	effective length (m)
h_{fg}	heat of vaporization (J kg^{-3})
N_g	acceleration multiplier (g)
$\Delta P_{\parallel}$	axial hydrostatic pressure drop (Pa)
$\Delta \mathrm{P}_{+}$	transverse hydrostatic pressure drop (Pa)
ΔP_c	capillary pumping pressure (Pa)
ΔP_{ph}	phase change pressure drop (Pa)
ρ_L	liquid density (kg m^{-3})
q_{out}	heat output (W)
ΔT	temperature difference (K)
R	thermal resistance (K W^{-1})
σ	surface tension (N m^{-1})
S	pillar width (M)

θ	liquid/solid contact angle (°)
T_e	average evaporator temperature (K)
T_c	average condenser temperature (K)
μ_L	liquid viscosity (N s m^{-2})
w	groove width (m)
W	liquid flow path width (m)
Δx	distance (m)

1. Introduction

The development of miniaturization and high-density packaging of electronic components has led to great challenges in thermal management. The demand for electronics cooling has increased steadily and predictably since Moore's concept [1]. Since then, various strategies have been used to remove the waste heat produced by integrated circuits, including heat spreading materials, liquid cooling, refrigeration and solid-state cooling [2]. Heat spreading materials may be simply high thermal conductivity materials such as copper, carbon fiber, various novel composites or more complex devices such as vapor chambers and heat pipes. Heat pipes have long been considered as an excellent solution and the conventional metallic cased, cylindrical heat pipes have been adapted for cooling of laptop microprocessors.

A heat pipe is an enclosed vessel that is equipped with a liquid wicking structure and that contains a fluid in the liquid and vapor phases. Heat entering one region of the vessel vaporizes the liquid lining in the inner wicking structure and the vapor is transported to a cooler region where it then condenses. The heat of vaporization is then extracted to a heat sink and the condensate is drawn back to the evaporating region due to the capillary pumping pressure of the inner liquid wicking structure.

There have been great interests in developing heat pipes that are nonmetallic. Jones *et al* [3] developed a nonmetallic heat pipe using a rigid ceramic substrate. The challenge with this nonmetallic casing material was its high thermal resistance. By using silver-filled thermal vias through the ceramic, they were able to increase the effective thermal conductivity from 2.63 W (m K)$^{-1}$ to 250 W (m K)$^{-1}$ for the casing material. Wits *et al* [4] utilized rigid PCBs and axially oriented micro-grooves formed with a selective plating process. They too used metal-filled thermal vias to decrease the casing's thermal resistance. With a 10 W heat input to their device, the resulting overall thermal resistance was 1.4 K W^{-1} at horizontal orientation and 1.0 K W^{-1} at vertical orientation (with gravity assisting). The prospects of a flat, flexible heat spreader were explored in 2007 by Hilderbrand *et al* [5]. Their application was the treatment of neocortical epilepsy by cooling specific regions of the human brain. Although the analysis suggested that the application would have been successful, their attempt to fabricate a heat spreader from the polyethylene film was not realized.

A critical component of heat pipes is the wicking structure. Liquid wicking structures have been fabricated in many different ways and using many different materials. Photolithography combined with electroplating has recently been an attractive method of realizing heat spreader liquid wicking structures due to the small-scale precision of placement and ability to define widely varying geometries. In 2002, Cheng *et al* [6] utilized the LIGA technique to define very high aspect ratio nickel groove structures that were 1 mm deep and 100 μm wide. Although modeled and fabricated, the wicking structures were not tested for any practical application. Joo *et al* [7] in 2008 used a much simpler technique to create liquid flow channels. Instead of the traditional LIGA process which requires a high-power synchrotron, they used an easily definable and removable photoresist to create 43 μm high nickel channels with 5 μm width. This structure was however applied to forced gas convection fins and not to heat pipes. The same technique was used recently by Nam *et al* [8] to fabricate 50 μm diameter copper post-wicking structures using an epoxy-based photoresist. Excellent wicking ability was demonstrated after a chemical oxidation treatment. In our previous work [9], we developed a polymer-based flat heat pipe utilizing polymer film as a casing material, micro-fabricated copper-filled thermal vias, and hybrid wicking structure consisting of wet-etched grooves and woven copper mesh. The device was 30 × 60 × 1 mm^3 and transferred a heat flux up to 11.94 W cm^{-2} with an effective thermal conductivity of 830 W (m K)$^{-1}$.

Modern mobile electronic devices must be cooled in any orientation with respect to gravity. The dynamic impact could be even more severe for military electronics. Hence, wicking structures must be able to function against the hydrostatic pressure drop caused by gravitational acceleration. The copper heat pipe developed by Lim *et al* [10] was tested both horizontally (0 *g*) and vertically (1 *g*) and the laser formed copper wicking grooves proved viable liquid wicking in both orientations. Chamarthy *et al* [11] assessed the wicking ability of 75 μm diameter sintered copper particles from 0 to 10 *g*. They used an ultraviolet fluorescent flow visualization method with a centrifuge to determine the effect of acceleration on the ability of the liquid wicking structure to retain water. It was found that the sintered particles held water but the UV intensity (quantity of liquid) decreases with both height and acceleration. Ding *et al* [12] also assessed a liquid wicking structure made of micro-scale titanium pillars with a nano-scale surface treatment under the influence of high acceleration. They found that bitextured titanium pillars were able to hold liquid up to 12.13 *g* acceleration while the plain pillars dried out at 6.3 *g* acceleration. The thermal performance of an oscillating heat pipe under high acceleration has been reported by Thompson *et al* [13]. Unlike a traditional heat pipe, the oscillating heat pipes do not rely on a liquid wicking structure to move liquid from the condenser to the evaporator but rather used the oscillating movement of liquid and vapor slugs to transfer heat. Their copper device transferred 95 W with a nearly constant effective thermal conductivity of about 700 W (m K)$^{-1}$ from 0 to 10 *g* acceleration. A flat copper/water heat pipe was fabricated and tested by de Bock *et al* [14]. They used a similar sintered copper powder wicking structure as that in [11]. The experimental data showed an effective thermal conductivity of 260–360 W (m K)$^{-1}$ with 10 W power input from 0 to 10 *g*. The power input was then increased to about 40 W and the effective thermal conductivity generally remained constant around 260 W (m K)$^{-1}$.

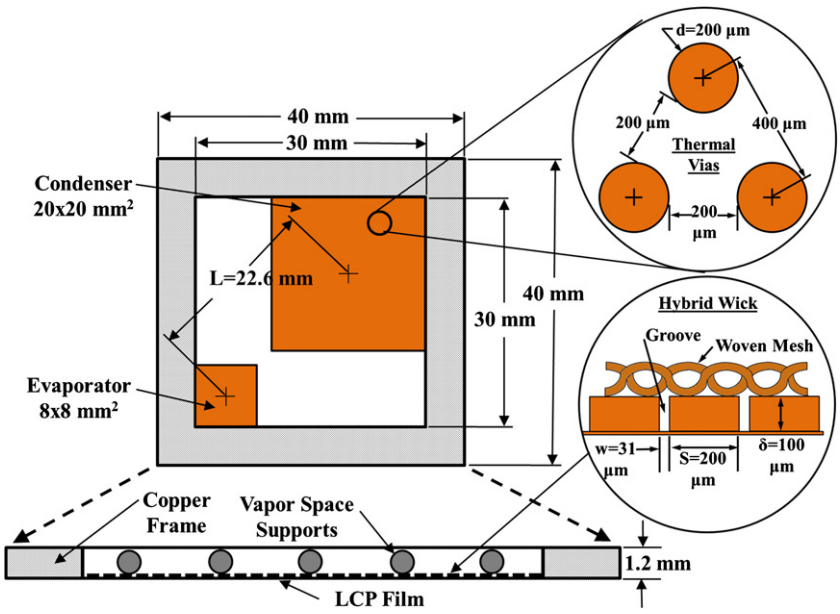

Figure 1. Top and cross-sectional views showing the overall geometry of the polymer heat spreader and location of the evaporator and condenser regions.

The objectives of this work are twofolds: (1) to develop a flat heat pipe that is polymer based, rather than metallic, manufacturable with standard PCB technologies and for use as a heat spreader in a flexible circuit board, and (2) to assess the thermal performance of such polymer-based flat heat pipe spreaders at an adverse acceleration up to 10 *g*.

In the following, we describe the fabrication, assembly and testing of a $40 \times 40 \times 1.2$ mm^3 polymer-based flat heat pipe heat spreader. It utilized grooves formed with high aspect ratio copper micro-pillars and topped with a copper woven mesh to form a hybrid wicking structure. Copper-filled thermal vias were placed throughout the casing to reduce the thermal resistance through the liquid crystal polymer film. Water was used as the working fluid. An analysis was performed to predict the dry-out point of the device in terms of power input and acceleration. The flat heat pipe heat spreader was tested with input heat fluxes ranging from 7.8 to 63 W cm^{-2} (5–40 W) and with adverse acceleration ranging from 0 to 10 *g*.

2. Design, fabrication and assembly

The overall geometry of the flat heat pipe heat spreader is shown in figure 1. The external size of the device was $40 \times 40 \times 1.2$ mm^3 with an inner vapor chamber of $30 \times 30 \times 1.0$ mm^3. An 8×8 mm^2 evaporator area was located at one corner while a 20×20 mm^2 condenser area was located at the opposing corner giving an effective length (L) of 22.6 mm from the center of the evaporator to the center of the condenser. Liquid crystal polymer (LCP) was chosen as the casing material for the flat heat pipe due to several reasons including chemical resistance, customizable CTE, low moisture absorption and its prevalence as a standard flexible printed circuit board (PCB) material [15].

Copper-filled thermal vias with a diameter of 200 μm and pitch of 400 μm span the entire 30×30 mm^2 area. The fabrication details of these thermal vias were reported in [9]. The hybrid wicking structure, which enhances evaporation and condensation heat transfer under adverse acceleration, consists of 100 μm high (δ), 200 μm wide (S) square electroplated copper micro-pillars with 31 μm wide grooves (w) for liquid flow and a woven copper mesh with 51 μm diameter wires and 76 μm spacing bonded to the top surface of the pillars. Water was chosen as the working fluid for several reasons due to its superior properties such as high latent heat of vaporization, low liquid viscosity, high liquid density and high surface tension. Furthermore, water presents low toxicity in the event of a catastrophic rupture of the device. All calculations in the rest of this paper utilize water properties at 313 K.

2.1. Design rationale

The flat heat pipe heat spreader performance was characterized under the dynamic forces of adverse acceleration (where the liquid must return to the evaporator against a force). If the heat spreader still functions under high acceleration, the maximum capillary pumping pressure, $\Delta P_{c,\max}$, of the wicking structure must be sufficient to overcome the pressure drops associated with viscous liquid loss, $\int_L \frac{dP_L}{dx} dx$, and hydrostatic loss, $\Delta P_{\parallel}$ as in the following equation [16]:

$$\Delta P_{c,\max} \geqslant \int_L \frac{dP_v}{dx} dx + \int_L \frac{dP_L}{dx} dx + \Delta P_{ph,e} + \Delta P_{ph,c} + \Delta P_{||}. \quad (1)$$

The other pressure losses; viscous vapor $\int_L \frac{dP_v}{dx} dx$, evaporation $\Delta P_{ph,e}$ and condensation $\Delta P_{ph,c}$ phase change have been found to be negligible compared to the liquid viscous and hydrostatic losses [17]. The hydrostatic pressure drop from the center of the evaporator to the center of the condenser is found by

$$\Delta P_{||} = \rho_L g L N_g = 220 N_g \quad (2)$$

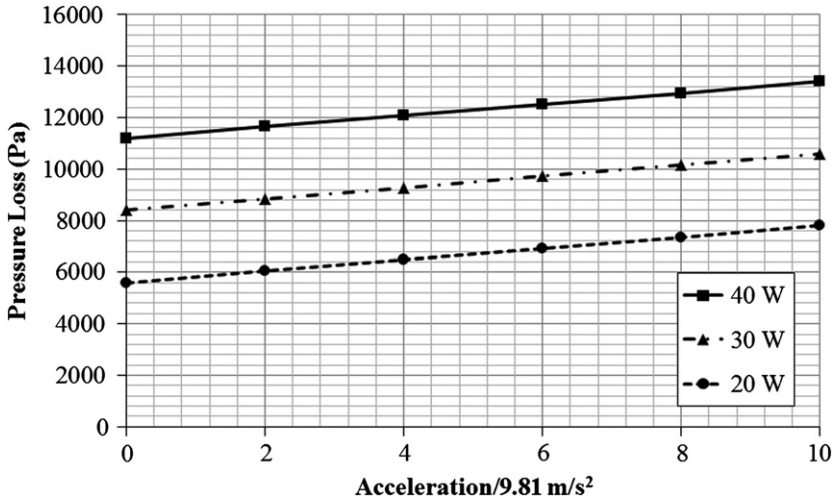

Figure 2. The relationship between the acceleration, the input power and the resulting pressure loss in the heat pipe heat spreader.

where ρ_L is the liquid density, g is the acceleration due to gravity, L is the heat spreader effective length and N_g is the multiplier of the g force for the acceleration. The hydrostatic pressure ranges from 0 to 2200 Pa at 0–10 g, respectively, for the effective device length of 22.6 mm.

In order to show the need in using a hybrid structure, the pressure drop and capillary force are found if only the micro-machined grooves are used as the liquid wicking structure. To simplify the calculation while still roughly determining an approximation of the liquid viscous pressure loss, we are assuming one-dimensional liquid flow through the wicking structure. The width of the liquid flow path is the average width of the evaporator and condenser ($W = 19.8$ mm) and the length of the flow path is the effective length from center to center. Integrating the second term on the right side of equation (1), representing the pressure drop due to viscous liquid losses, and then substituting relations for shear pressure, Reynolds number and liquid velocity result in the expression [16]

$$\Delta P_L = \left(\frac{\mu_L L}{K A_w h_{fg} \rho_L}\right) q \tag{3}$$

where μ_L is the liquid viscosity, L is the effective length, K is the groove permeability, A_w is the total cross-sectional area of the wicking structure represented by the product of the wick height and wick width ($A_w = \delta W$), h_{fg} is the latent heat of vaporization and q is the heat being transferred. This is a 1D form of Darcy's law for fluid flowing through a porous medium under steady-state conditions. In order to determine the permeability of the grooves of the wicking structure, the liquid friction factor was first evaluated by an empirical expression presented by Shah and Bhatti [18] for flow through rectangular grooves

$$f\mathrm{Re}_{L,h} = 24(1 - 1.3553\alpha + 1.9467\alpha^2 - 1.7012\alpha^3 + 0.9564\alpha^4 - 0.2537\alpha^5). \tag{4}$$

The liquid friction factor was determined using the reciprocal of the aspect ratio, $\alpha = \mathrm{w}/\delta$, where w is the groove width (31 μm) and δ is the groove height (100 μm). The given groove geometry results in $\alpha = 0.31$ and the liquid friction factor is then 17.4 [18]. The permeability of the grooves can be found from [16]

$$K = \frac{D_h^2 \varepsilon}{2(f\mathrm{Re}_{L,h})} \tag{5}$$

where D_h is the hydraulic diameter and ε is the porosity. The hydraulic diameter of the grooves is

$$D_h = \frac{4A}{P} = \frac{4\delta w}{2\delta + w} \tag{6}$$

where A is the cross-sectional area and P is the wetted perimeter of the groove, and was calculated to be 53.7 μm. The porosity is the ratio of the open flow area to the total area or $\varepsilon = \delta w/\delta(W+w)$. The given groove geometry results in a porosity of 0.134, and with the previously calculated liquid friction factor, the calculated permeability of the groove structure is $1.11 \times 10^{-11}\,\mathrm{m}^2$. The liquid viscous pressure drop may now be determined from equation (3) using the wick cross-sectional area of $1.98 \times 10^{-6}\,\mathrm{m}^2$ to be

$$\Delta P_L = 280q. \tag{7}$$

This expression is directly dependent on the heat being transferred, q, as more heat requires a larger flow rate and hence higher fluid velocity and viscous pressure loss. Figure 2 shows the calculated pressure drops associated with various acceleration loadings and power inputs.

The maximum pressure loss occurs at the maximum acceleration and heat load, which in the current testing occurs at 10 g and 40 W, respectively. The capillary pumping pressure must therefore be equal to or greater than the maximum sum of those two pressure losses, or 13 400 Pa, for the heat spreader to function under these conditions.

The maximum capillary pumping pressure offered by the given groove geometry is determined from the Young–Laplace relation [16]

$$\Delta P_{c,\max} = \frac{2\sigma \cos\theta}{r_c}. \tag{8}$$

Assuming the ideal case of perfect wettability where the liquid contact angle θ is 0°, the surface tension of the water at 313 K is $70 \times 10^{-3}\,\mathrm{N\ m^{-1}}$, and the capillary radius, $r_c = w$ (for grooves), is 31 μm, the resulting capillary pumping

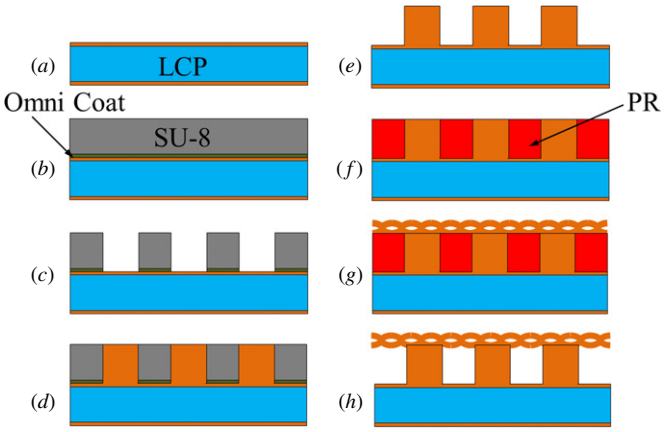

Figure 3. Fabrication process for the hybrid wicking structure composed of high aspect ratio copper pillars and a bonded woven mesh for the flat heat pipe heat spreader.

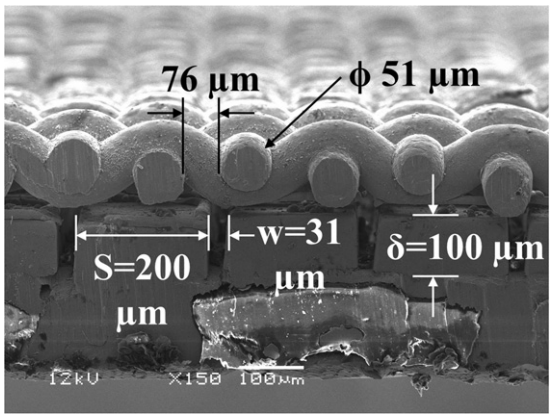

Figure 4. SEM image of the hybrid wicking structure consisting of a woven copper mesh bonded the top surface of 100 μm high electroplated copper pillars.

pressure is 4516 Pa. Clearly, the grooves alone are theoretically not able to supply enough liquid to the evaporator during the operation with high power and high acceleration. Thus, additional microstructure modifications were needed to meet the requirements of 10 *g* acceleration with 40 W power input. In this work, we decided to bond a woven copper mesh with 51 μm diameter wires and 76 μm spacing on the top surface of the micro-pillars as hybrid wicking structures. It is expected that the liquid meniscus at the interface between the top of the pillar structures and the woven mesh can develop a smaller capillary radius and display a much stronger capillary pumping pressure than the grooves.

2.2. Fabrication of a hybrid wicking structure

The goal of this fabrication process was to create a hybrid wicking structure consisting of high aspect ratio micro-pillars with woven mesh bonded to the top surface. The advantage of a hybrid wicking structure is that the grooves formed by the pillars allow flow with low viscous losses as the liquid moves from the condenser to the evaporator. The woven mesh or the smaller capillary radius developed at the interface between the top of the pillar structures and the woven mesh could provide a strong capillary pumping pressure. The hybrid structure also provides effective evaporative and condensing surfaces. This work differs significantly from Oshman *et al* [9] by forming sharp corners in the copper microchannels, which has been demonstrated by Peterson [19] to greatly enhance capillary pumping ability compared to larger radius corners formed by a process such as isotropic wet etching reported in [9].

The substrate on which this structure was formed is a 100 μm thick liquid crystal polymer film with a 18 μm copper thin film on both sides (Roger's Corp. Ultralam 3850) shown schematically in figure 3(*a*). This flexible substrate was bonded to a rigid 10 cm diameter silicon wafer to hold it flat for processing. First, a 50 nm layer of Microchem Omnicoat was spin coated onto the substrate. This layer allows later removal of the next layer of 100 μm thick epoxy-based negative photoresist (Microchem SU-8) as in figure 3(*b*). The SU-8 and Omnicoat were patterned to form 200 μm wide pillar molds with 31 μm spacing (figure 3(*c*)). After O_2 plasma treatment to clean the now exposed copper surfaces, pillars were formed through the SU-8 mold with a copper electroplating process (figure 3(*d*)). The electroplating process was optimized to create uniform high aspect ratio micro-pillars that are not overplated beyond the height of the SU-8 layer. The bulk of the SU-8 was then softened and released by immersion in Microchem Remover PG (figure 3(*e*)). Even after prolonged exposure to the Remover PG, some residue of SU-8 still remained. The remainder was then completely removed through SF_6/O_2 reactive ion etching. The result was high aspect ratio micro-pillars with very small radius corners at the base as shown in figure 4.

The next step was to bond the woven copper mesh to the top surface of the pillars which begun by filling the grooves completely with an easily removable photoresist (AZ-P4620) as shown in figure 3(*f*). After filling the grooves, the top surface was finely polished to expose just the top surface of the pillars. The woven copper mesh, with a wire diameter of 51 μm and a spacing of 76 μm, was then applied to the sample, pressed with uniform pressure and bonded with another copper electroplating process as in figure 3(*g*). The application of PR in the grooves ensured that the desired sharp base corners remained intact during electroplating. This plating process occurred long enough for the mesh to strongly bond to the top pillar surface but not long enough that the mesh geometry was severely altered. The final step was to completely dissolve the PR from the inside of the channels with solvent as in figure 3(*h*).

The pillars fabricated by the electroplating and SU-8 molding method described above resulted in very sharp corners at the base of the channels which is most desirable for liquid capillary wicking. Finally, the copper-filled thermal vias are fabricated as described in detail in [9].

2.3. Assembly

The completed LCP film with copper-filled thermal vias and copper hybrid wicking structure was soldered onto a 5 mm wide and 1 mm thick copper frame and topped with a $4 \times 4\,cm^2$ copper foil. An array of 1 mm stainless steel spheres

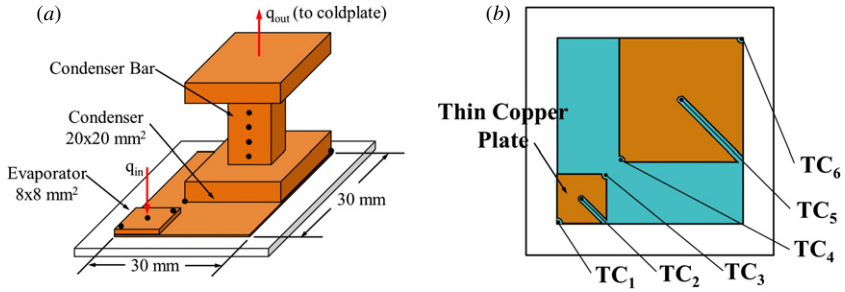

Figure 5. Schematic diagram of (*a*) the experimental apparatus used to assess the performance of the flat polymer heat spreader and (*b*) the location of TCs on the heat spreader.

were bonded to the top foil to avoid the collapse of the flexible material under atmospheric pressure differential and to provide adequate vapor transport space during the operation of the device as shown at the bottom of figure 1. A copper tube was assembled into the frame for the purpose of evacuation and charging. Evacuation was accomplished with a turbo-molecular vacuum pump to a pressure level of 1.0×10^{-6} Torr and held for several hours with heating to induce outgassing from the inside surfaces.

Once evacuation was complete, the device was charged with 0.247 ml of distilled and degassed water using a backfill technique [9]. The amount of water charged was determined experimentally for optimum performance of the device. After charging, the copper tube was cold welded and the end of the tube sealed with Torr–Seal vacuum epoxy.

3. Experimental characterization and data reduction

3.1. Experimental characterization

In order to assess the thermal performance of the polymer-based flat heat pipe heat spreader, its operational temperature distribution was compared to that of a sample with known thermal conductivity and equivalent external geometry, which in this case was a reference copper block. Heat was applied to the evaporator region using a ceramic heater (Watlow Ultramic) over an 8×8 mm^2 area located at one corner of the device as shown in figure 5(*a*). The power input was calculated as the product of the current and the voltage supplied to heater. Three k-type thermocouples (TCs, ± 0.1 K) were bonded to the surface of the evaporator region with thermal epoxy (Omegabond 101) and three were bonded to the condenser surface as shown in figure 5(*b*).

A thin 8×8 mm^2 copper plate was used to place the ceramic heater for heat input to the flat heat pipe heat spreader where the inner heating area of the heat spreader could be called the evaporator surface. Channels were formed into the copper plate to allow clearance of the TCs as shown in figure 5(*b*). A highly insulated solid aluminum bar was placed in contact with the heat spreader surface on the corner opposite to the evaporator area (the heater area). Each end of the solid aluminum bar was 20×20 mm^2 and one end had TC clearance grooves also shown in figure 5(*b*). The inner cooling area of the heat spreader is called the condenser surface. The other end of the bar was placed in contact with an aluminum cold plate with constant 283 K chilled water flow. The solid aluminum

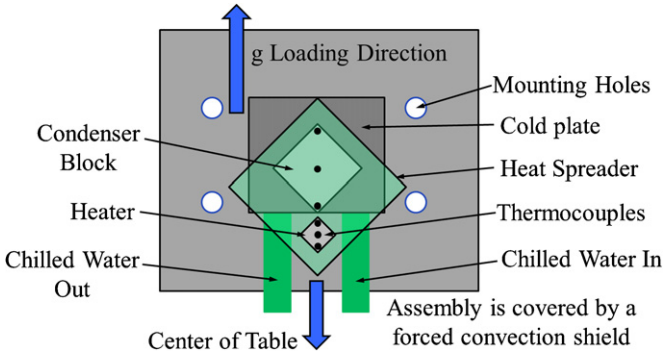

Figure 6. Illustration of the cold plate and device orientation on the rotation table.

bar served as the heat sink for the heat spreader. An equally spaced linear array of four k-type TCs embedded in the center of the 10×10 mm^2 condenser bar provided a measure of the actual heat flux being extracted, q_{out}, from the condenser of the heat spreader using the following equation

$$q_{out} = k_{Al} A_{Al} \frac{\Delta T_{Al}}{\Delta x} \tag{9}$$

where k_{Al} is the thermal conductivity of the aluminum condenser bar, A_{Al} is its cross-sectional area, ΔT_{Al} is the average temperature difference along its length and Δx is the distance between TCs.

The apparatus shown schematically in figure 6 was used to experimentally evaluate the heat spreader under dynamic acceleration conditions and provide and extract heat.

The solid aluminum bar was clamped to a cold plate and the heater was clamped to the heat spreader and each interface was coated with a thin layer of thermally conductive paste (Omega OT-201) which served as a thermal interface material. The entire apparatus was mounted to the centrifuge shown in figure 7.

This centrifuge allowed experimental evaluation of both the copper reference sample and the heat pipe heat spreader with the application of adverse radial acceleration, where the condensate must return to the evaporator against the acceleration force. The radial acceleration was varied from 0 *g* to 10 *g* (0–98.1 m s^{-2}) in increments of 2 *g* and held for 3 min each. The electrical power input to the heater was 20, 30 and 40 W. Electrical and TC connections were provided by a slip-ring system and chilled water was supplied and removed from the cold plate with a fluidic rotary union.

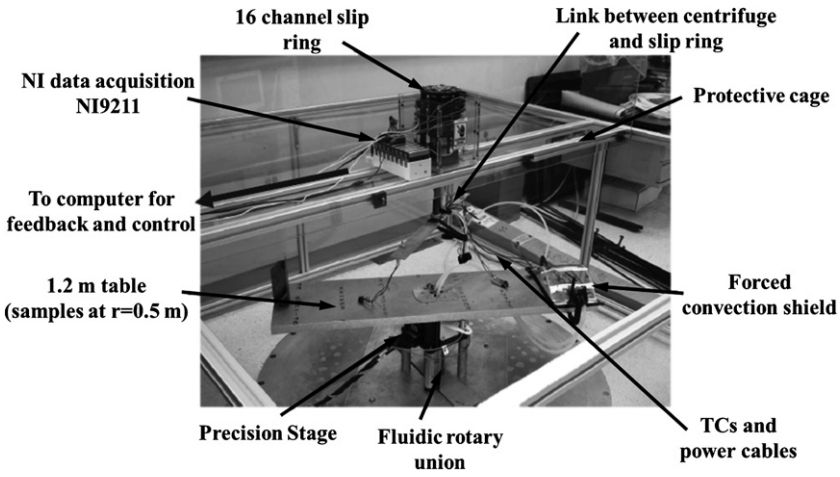

Figure 7. Photograph of the centrifuge used to apply acceleration forces to the heat spreaders.

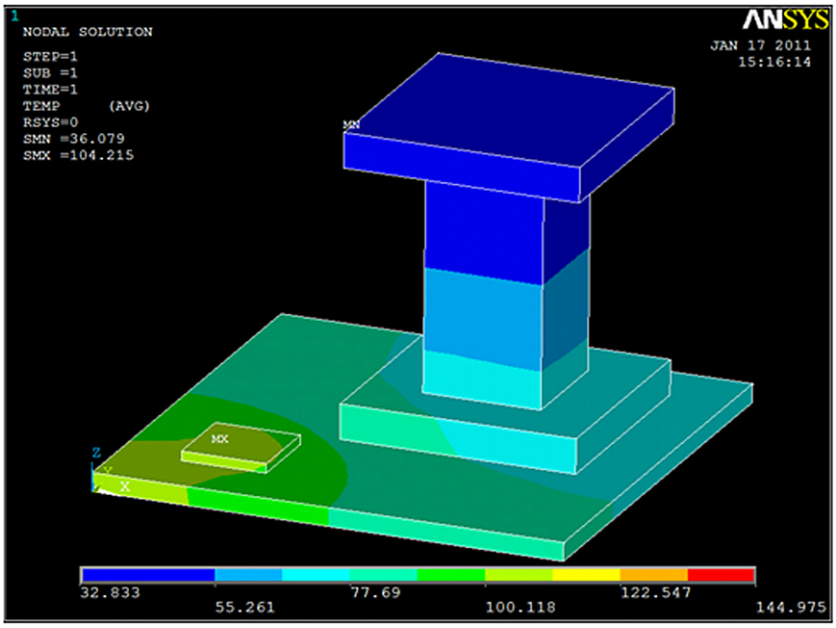

Figure 8. Resulting FEA temperature distribution of the copper reference sample, thin copper heater plate and aluminum condenser bar with 30 W power input.

The copper reference sample and the flat heat pipe heat spreader were both evaluated in the centrifuge testing fixture. An acrylic shield was placed around the test samples to avoid excessive heat loss from forced convection due to the extreme velocity of up to 22 m s^{-1} required to reach the required acceration magnitude. Measuring the thermal resistance of the copper reference sample with dynamic acceleration confirmed negligable heat loss due to forced convection while using the convection shield.

3.2. Data reduction

To extract the effective thermal conductivity of the heat pipe heat spreader from the measurement of temperature distributions, the experimental temperature distribution of the sample was compared to the temperature distribution obtained from a finite element analysis (FEA). The FEA modeling geometry was identical to the experimental sample's geometry. The temperature distribution of the copper reference sample calculated with FEA for 30 W power input is shown in figure 8 along with the thin copper plate and the aluminum condenser bar.

The key to data reduction is to determine the heat loss to the environment through natural convection. This goal was accomplished by the detailed comparison of the copper reference sample under different heat inputs and accelerations. With known thermal conductivity of the copper reference sample and the thin copper plate (391 W (m K)$^{-1}$) and aluminum (167 W (m K)$^{-1}$), the natural convection heat transfer coefficients were adjusted in the FEA to match the experimentally measured temperature distribution. The natural convective heat transfer coefficients were found to be 10 W (m^2 K)$^{-1}$ for the top surface of the heat spreader, 8 W (m^2 K)$^{-1}$ for the bottom surface of the heat spreader and 4 W (m^2 K)$^{-1}$ for the surface of the aluminum bar. Due to the relatively small

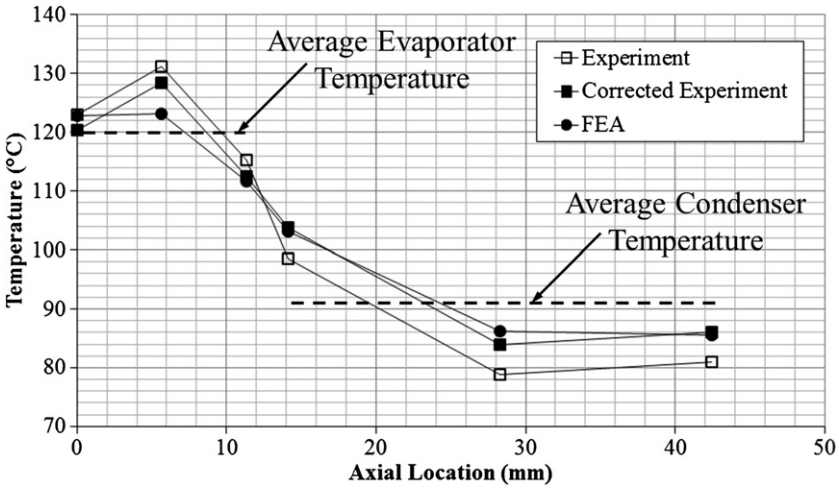

Figure 9. Simulated and experimental diagonal temperature distribution of the copper reference sample at 40 W power input showing a good agreement.

heat loss from natural convection (<4%) owing to the good insulation even under high acceleration and the large thermal conductivities of the test samples, the boundary conditions were held constant in all the cases for both the copper samples and the heat pipe heat spreaders.

Figure 9 shows the diagonal temperature distribution of the copper reference sample at each TC location for the experimentally measured data and that obtained by the FEA at 40 W power input. The data shown are discontinuous and the lines connecting the points are for illustration purposes only.

The deviation seen between the experiment and the FEA values indicated that the surface-mounted TCs experienced excessive surface heating and cooling effects due to proximity contact with the heater element and the condenser bar and did not represent the true surface temperature measurement. This was confirmed when TCs were embedded at identical locations but slightly below the surface of the copper reference sample to observe the extent of the surface heating and cooling effects. In addition, heat spreading occurred along the 5 mm outside border of the copper reference sample. This further decreased the outside temperature of the evaporator region. That data were then used to determine the magnitude of temperature offset required to negate the effect of direct TC contact with the heater and cooling block. After offsetting a uniform, power-dependent average temperature (-0.075 q for the evaporator and $+0.2$ q for the condenser), the average evaporator temperature and condenser temperature agreed very well between the model and the experiment.

The same natural convection heat transfer coefficients were used to simulate the temperature distribution of the heat pipe heat spreader where the thermal conductivity of the heat spreader material was an input variable that varied from 390 W (m K)$^{-1}$ to 2000 W (m K)$^{-1}$. This analysis was used to determine the effective thermal conductivity of the heat pipe heat spreader under various power input and acceleration loadings by matching the average evaporator and condenser temperature between the experimental data and the FEA simulations.

4. Results and discussions

The data collected from each experiment were in the form of the temperature of three thermocouples on the evaporator side (k-type ± 0.1 K), three TCs on the condenser side, four TCs in the solid aluminum bar as a function of the electrical power input to the heater and the acceleration force in terms of g. Figure 10 shows the temperature difference (ΔT) between the average of the evaporator TCs and the condenser TCs for the copper reference sample and the flat heat pipe heat spreader at 20, 30 and 40 W power input under different accelerations.

Power was applied to the heating element and the samples were held in a stationary horizontal position (0 g) for 8 min. The centrifuge then began rotation and was stepped through 2, 4, 6, 8 and 10 g acceleration. Each rotational speed was maintained for 3 min and then the sample rotation was stopped after 10 g. The temperature difference (ΔT) offered a measure of the performace characteristics of the heat spreader materials. Small ΔT indicated a low thermal resistance and high effective thermal conductivity while a large ΔT indicated a high thermal resistance and low effective thermal conductivity. The copper reference sample exhibited ΔT that was independent of acceleration and which varied from a minimum of 14.5 K W^{-1} at 20 W heat input to a maximum of 29.2 K W^{-1} at 40 W heat input. The heat pipe heat spreader showed lower ΔT values compared to the copper reference sample at all power levels up until 10 g acceleration for 30 and 40 W. At 20 W power input, the heat spreader ΔT decreased slightly as the acceleration began and rose significatly only at 10 g acceleration. It is suspected that this is due to the acceleration force extracting excessive liquid from the flooded evaporator to the condenser side allowing a more efficient evaporation from the surface of the hybrid wicking structure. At power levels of 30 and 40 W, ΔT increased steadily with each step increase of acceleration because the flooded evaporator condition is mitigated due to the higher heat flux. The temperature difference returned close to the starting point after the acceration phase was completed for all power levels. The propagated uncertainty for the ΔT measurements was composed of three linear combinations

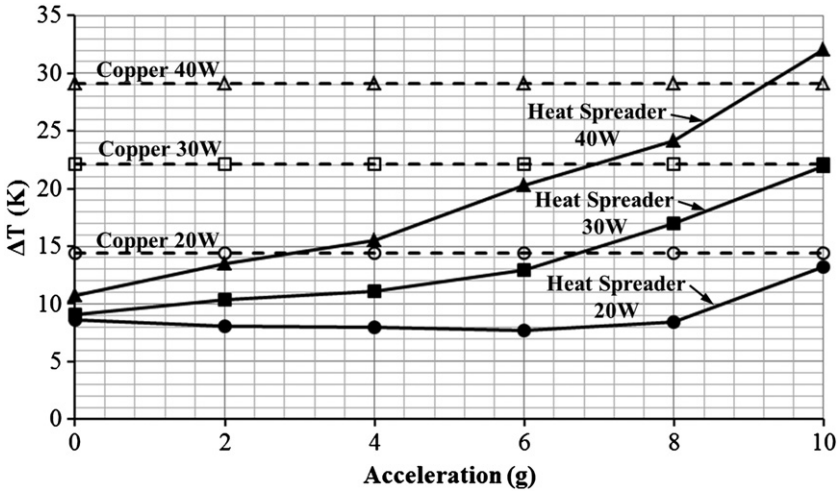

Figure 10. Measured temperature difference between the evaporator and the condenser of the copper reference sample and the heat pipe heat spreader with 20, 30 and 40 W heat input and under 0–10 *g* acceleration.

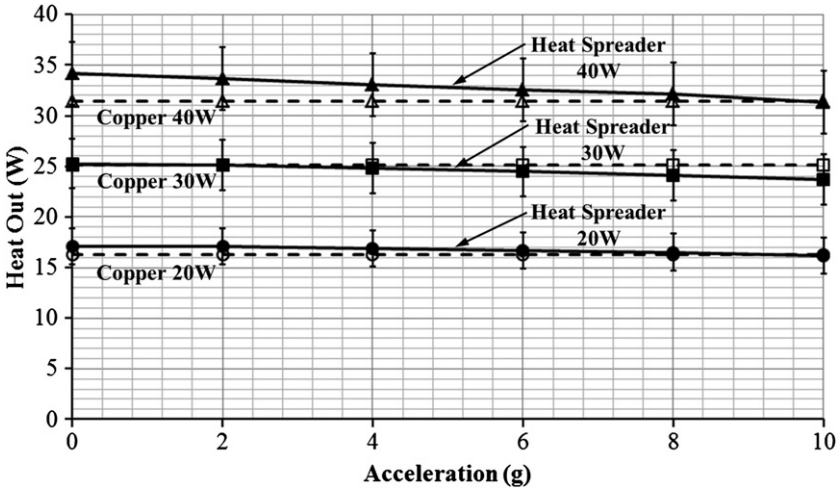

Figure 11. Measured heat output through the copper reference sample and the heat pipe heat spreader with 20, 30 and 40 W heat input and under 0–10 *g* acceleration.

(T_e, T_c and ΔT) and was calculated to be ± 0.336 K with a confidence level of 95% based on the natural variability of the thermocouple signal.

Due to the heat losses through natural convection, the power input to the heater cannot be directly used for calculating the effective thermal conductivity or thermal resistance. The heat extracted from the copper reference sample and heat pipe heat spreader was then determined using equation (9) with a 1-D array of four k-type thermocouples embedded along the length of the solid aluminum bar. Figure 11 shows the heat, q_{out}, transferred by both the copper reference sample and the heat pipe heat spreader where the *x*-axis is the acceleration magnitude.

The copper sample and heat pipe heat spreader exhibited similar quantities of heat transferred for each power level. Acceleration seemed to display a relatively small effect on this quantity with a change of 5.8%, 6.3% and 8.5% at 20, 30 and 40 W, respectively. Since the copper reference sample displayed no change with acceleration, it can be surmised that the higher acceleration impeded the heat pipe heat spreader condensate return to the evaporator with an increase in hydrostatic pressure. The combination of high viscous losses at 40 W power input and the 10 *g* acceleration of the heat spreader shows the highest decrease in the heat transferred. The propagated uncertainty of the q_{out} calculation is shown in the figure and was composed of one linear and two nonlinear combinations ($\Delta T_{\text{Al, avg}}$, A_{Al} and q) and ranged from ± 1.79, 2.46 to 3.10 W for 20, 30 and 40 W heat input, respectively.

As mentioned in section 3.2, FEA was used to determine the effective thermal conductivity of the heat pipe heat spreader. Often, the thermal conductance or thermal resistance is used in the literature to characterize the thermal performance of heat pipes and vapor chambers. The overall thermal resistance of the heat pipe heat spreader can be defined by using the average evaporator temperature T_e, q_{out}, and the average condenser temperature T_c:

$$R = \frac{T_e - T_c}{q_{\text{out}}} = \frac{\Delta T}{q_{\text{out}}}. \tag{10}$$

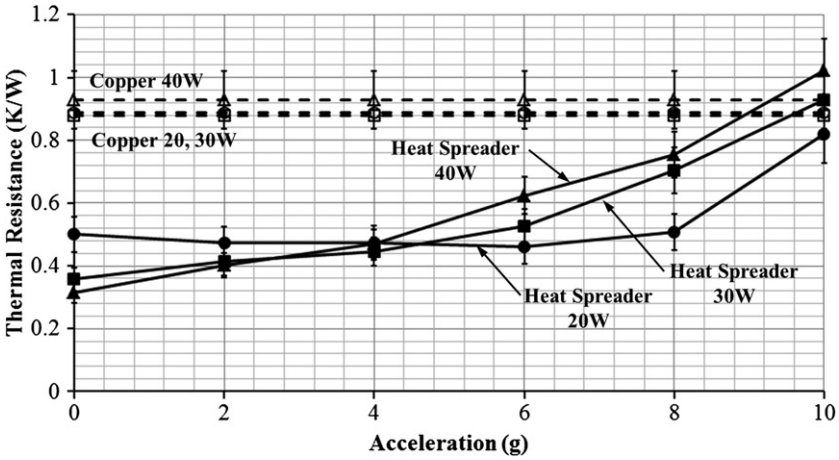

Figure 12. Measured thermal resistance of the copper reference sample and the heat pipe heat spreader with 20, 30 and 40 W heat input and under 0–10 *g* acceleration.

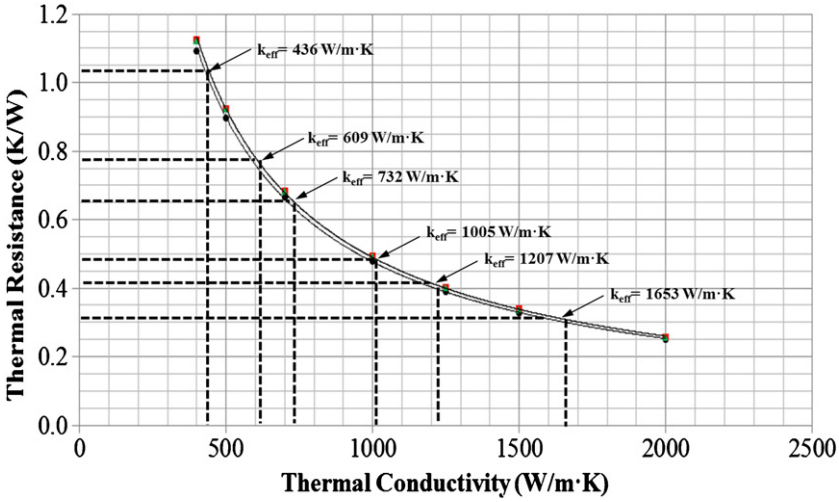

Figure 13. Plot displaying the FEA-derived curves showing the dependence of effective thermal resistance on the effective thermal conductivity at 20, 30 and 40 W power input. Shown are the test results of the heat pipe heat spreader at 40 W.

It is noted that the heat spreaders being evaluated in this testing transfer heat two dimensionally rather than purely axially and hence this relation for effective thermal resistance is for the convenience of data presentation only.

Figure 12 shows the thermal resistance, R, calculated from results for ΔT and q_{out} shown in figures 10 and 11.

The effective thermal resistance of the copper reference sample showed a constant value of 0.88 K W^{-1} for 20 and 30 W power input and 0.93 K W^{-1} for 40 W power input. The difference in thermal resistance when the heat input is higher is attributed to an increase in heat loss from convection and radiation due to higher sample temperatures. It can be seen that the trend for the heat pipe heat spreader thermal resistance is similar to that of the ΔT data where there is an increase for each step increase of the acceleration. The thermal resistance of the heat spreader generally increased as the power and acceleration were stepped up. The increase of power input increased the liquid mass flowrate through the wicking structure and therefore increased the viscous pressure loss. Also, the increase in acceleration lead to an increase in the axial hydrostatic pressure change. Each increase in the acceleration force and power input decreased the excess capillary pumping pressure provided by the wicking structure and this is observed as an increase of thermal resistance. The propagated uncertainty of the thermal resistance measurements shown in the figure is composed of one nonlinear combination and was found to vary from a minimum of ± 0.0413 K W^{-1} at 20 W and 0 *g* to a maximum of ± 0.129 K W^{-1} at 40 W and 10 *g*.

As detailed earlier, the heat pipe heat spreader presents two-dimensional heat transfer characteristics. After the case studies by FEA throughout the 20–40 W power input range, the relation between the effective thermal resistance and the effective thermal conductivity is presented by a set of nonlinear curves as shown in figure 13.

The three power fit plots between the effective thermal conductivity and the effective thermal resistance calculated using equation (10) were generated from the FEA results corresponding to 20, 30 and 40 W power input. The measured thermal resistance values of the heat pipe heat spreader are located on the vertical axis while the resulting effective thermal conductivities are located on the horizontal axis. This relation allowed determination of the effective thermal conductivity

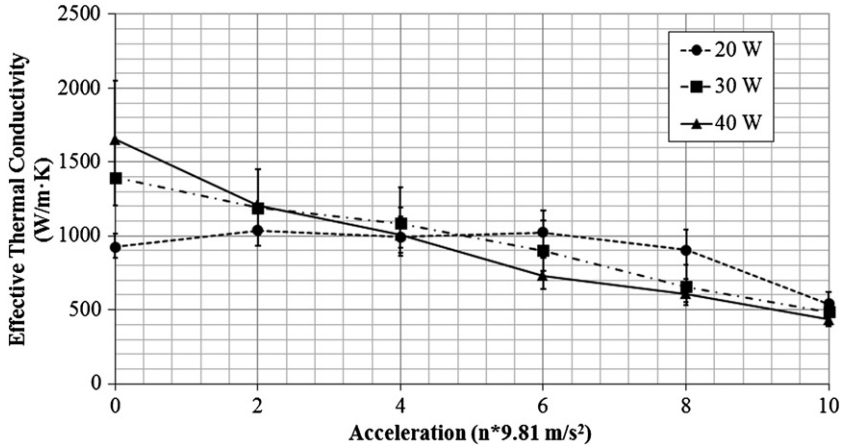

Figure 14. Summary of the resulting effective thermal conductivities for the heat pipe heat spreader at 20, 30 and 40 W power input for accelerations from 0 *g* to 10 *g*.

of a test sample given its measured thermal resistance. A summary of the thermal conductivity values derived from the R/k relations shown in figure 13 is plotted in figure 14 for the heat pipe heat spreader for 20, 30 and 40 W heat input powers.

This plot summarizes the effective thermal conductivities (k_{eff}) for all three power input levels under 0–10 *g* acceleration of the heat pipe heat spreader. The highest achieved thermal conductivity was 1653 W (m K)$^{-1}$ at 0 *g* with 40 W heat input. The lowest value reached was 436 W (m K)$^{-1}$ at 10 *g* with 40 W heat input. k_{eff} for 30 and 40 W power input decreased steadily when the acceleration increased from 0 *g* to 10 *g*. It is apparent that the flat heat spreader was still functional at 10 *g* acceleration and with 40 W power input. At 20 W power input, k_{eff} began at 925 W (m K)$^{-1}$, increased to 1037 W (m K)$^{-1}$, and then dipped down to 541 W (m K)$^{-1}$ at 10 *g* acceleration. As stated earlier, it is speculated that the movement of excess liquid from the initially flooded evaporator region toward the condenser region due to acceleration force is observed as an increase in k_{eff}. The removal of excess liquid decreased the capillary radius of the liquid meniscus in the grooves and therefore increased the capillary pumping pressure. This also allowed for more efficient evaporation in the hybrid wicking structure as more of the mesh surface was exposed.

The heat pipe heat spreader exhibited heat removal behavior at 10 *g* acceleration comparable to that of the copper reference sample. It may then be said that the capillary pumping pressure generated by the liquid wicking structure was sufficeint to overcome the sum of the viscous liquid and hydrostatic pressure drops. The maximum capillary radius required to function at these experimental parameters may be calculated. It was seen earlier that the maximum liquid pressure loss occurred at 40 W heat input and 10 *g* acceleration. The calculated total pressure drop of 13 400 Pa was due to viscous liquid loss and hydrostaic pressure loss. From equation (8), the capillary radius required to overcome this pressure drop is 10.4 μm while the existing groove capillary radius is 31 μm. Clearly, the liquid meniscus at the interface between the top of the pillar structures and the woven mesh developed a smaller capilary radius and hence displayed a stronger capillary pumping pressure than the grooves.

5. Conclusion

The performance of a polymer-based flat heat pipe heat spreader with a hybrid wicking structure was assessed under various power and acceleration loadings. This heat spreader was fabricated on a flexible polymer substrate in which copper-filled thermal vias were formed to decrease the thermal resistance through the device casing. The hybrid liquid wicking structure consisted of grooves formed with high aspect ratio copper micro-pillars with a woven copper mesh bonded to the top surface. The overall size of the assembled flat heat spreader was 40 × 40 × 1.2 mm^3 with an internal vapor chamber of 30 × 30 × 1.0 mm^3 and its performance was assessed with power inputs ranging from 20 W to 40 W over an area of 0.64 cm^2 (31–63 W cm^{-2}). The capillary pumping capability of the hybrid wicking structure was assessed under adverse gravitation force ranging from 0 *g* to 10 *g* (0–98.1 m s^{-2}). The highest effective thermal conductivity demonstrated was 1653 W (m K)$^{-1}$. As expected, the effective thermal conductivity of the heat spreader generally decreased with heat input and acceleration force due to increased liquid viscous and hydrostatic pressure losses. However, the heat spreader performance remained higher than that of a geometrically identical copper reference sample in nearly all cases despite the prediction of failure at 40 W power input. These results illustrate that a hybrid liquid wicking structure formed from high aspect ratio micro-pillars and woven copper mesh may be an attractive choice for heat pipes to cool application that vary in orientation and gravitational acceleration.

Acknowledgments

This work was supported by the DARPA Thermal Ground Plane Program managed by Dr Thomas W Kenny and Dr Avram Bar-Cohen (N66001-08-C-2006). The microfabrication process described in this work was conducted in the Colorado Nanofabrication Laboratories, which is supported by the NNIN and the National Science Foundation under grant no ECS-0335765. The views expressed are those of the author and do not reflect the official policy or position of the Department of Defense or the US Government. The

authors thank Nick Marsiglia and Susan Song for assistance in fabrication.

References

[1] Moore G E 1965 Cramming more components onto integrated circuits *Electronics* **19** 114–17

[2] Mahajan R, Chiu C P and Chrysler G 2006 Cooling a microprocessor chip *Proc. IEEE* **94** 1476–86

[3] Jones W K, Liu Y and Gao M 2003 Micro heat pipes in low temperature cofire ceramic (LTCC) substrates *IEEE Trans. Compon. Packag. Technol.* **26** 110–15

[4] Wits W, Legtenberg R, Mannak J and Zalk B V 2007 Thermal management through in-board heat pipes manufactured using printed circuit board multilayer technology *Int. Electron. Manuf. Technol.* 55–61

[5] Hilderbrand J K, Peterson G P and Rothman S M 2007 Development of phase change heat spreader for treatment of intractable neocortical epilepsy *Heat Transfer Eng.* **28** 282–91

[6] Cheng Y, Ding P P, Sheu B Y and Chen P H 2002 High performance flat miniature heat pipes fabricated by UD-LIGA process *Microsyst. Technol.* **9** 23–4

[7] Joo Y, Yeh H C T, Dieu K and Kim C J 2008 Air cooling of a microelectronic chip with diverging metal microchannels monolithically processed using a single mask *J. Micromech. Microeng.* **18** 1–13

[8] Nam Y., Sharratt S, Byon C, Kim S J and Ju Y S 2010 Fabrication and characterization of the capillary performance of superhydrophilic cu micropost arrays *J. Microelectromech. Syst.* **19** 581–88

[9] Oshman C, Shi B, Li C, Yang R G, Lee Y C and Bright V M 2011 The development of polymer-based flat heat pipes *J. Microelectromech. Syst.* **20** 410–17

[10] Lim H T, Kim S H, Im H D, Oh K H and Jeong S H 2008 Fabrication and evaluation of a copper flat micro heat pipe working under adverse-gravity orientation *J. Micromech. Microeng.* **18** 1–8

[11] Chamarthy P, de Bock H P, Russ B, Chauhan S, Rush B, Weaver S E, Deng T and Varanasi K 2009 Novel fluorescent visualization method to characterize transport properties in micro/nano heat pipe wick structures *Proc. of the ASME 2009 InterPACK Conf. (San Francisco, CA, USA, 2009)* pp 1–7

[12] Ding C, Bozorgi P, Meinhart C D and MacDonald N C 2010 Tunable wetting of titanium and gold based wicking materials for use under high accelerations *Proc. of NSTI-Nanotech 2010* vol 1 pp 616–19

[13] Thompson S M *et al* 2011 Robust thermal performance of a flat-plate oscillating heat pipe during high-gravity loading *J. Heat Transfer* **133** 104504

[14] de Bock H P *et al* 2011 Development and experimental validation of a micro/nano thermal ground plane *Proc. of ASME/JSME 8th Thermal Engineering Joint Conf. AJTEC 2011 (Honolulu, HI, USA)* pp T10249–T10249-7

[15] Wang X, Engel J and Liu C 2003 Liquid crystal polymer (LCP) for MEMS: processes and applications *J. Micromech. Microeng.* **13** 628–33

[16] Fahgri A 1995 *Heat Pipe Science and Technology* (Washington, DC: Taylor & Francis)

[17] Peterson G P 1994 *An Introduction to Heat Pipes* (New York: Wiley)

[18] Shah R K and Bhatti M S 1987 *Laminar Convective Heat Transfer in Ducts, Handbook of Single-Phase Convective Heat Transfer* ed S Kakac, R K Shah and W Aung (New York: Wiley)

[19] Peterson G P, Duncan A B and Weichold M H 1993 Experimental investigation of micro heat pipes fabricated in silicon wafers *J. Heat Transfer* **115** 751–56